Int J Appl Earth Obs Geoinformation 67 (2018) 1–9

Contents lists available at ScienceDirect

Int J Appl Earth Obs Geoinformation

journal homepage: www.elsevier.com/locate/jag

Deformation at longyao ground fissure and its surroundings, north China plain, revealed by ALOS PALSAR PS-InSAR

Chengsheng Yang[a], Zhong Lu[b,*], Qin Zhang[a], Chaoying Zhao[a], Jianbing Peng[a], Lingyun Ji[c]

[a] College of Geology Engineering and Geomatics, Chang'an University, Xi'an, Shaanxi province, 710054, China
[b] Roy M. Huffington Department of Earth Sciences, Southern Methodist University, Dallas, TX 75275, USA
[c] Second Crust Monitoring and Application Center, CEA, China

ARTICLE INFO

Keywords:
North China plain
Ground fissure
PS-InSAR
Fault modeling
Groundwater

ABSTRACT

The Longyao ground fissure (LGF) is the longest and most active among more than 1000 ground fissures on the North China Plain. There have been many studies on the formation mechanism of the LGF, due to its scientific importance and its potential for damage to the environment. These studies have been based on both regional tectonic analysis and numerical simulations. In order to provide a better understanding of the formation mechanism, the deformation of the crack and its surrounding environment should be taken into consideration. In this paper, PS-InSAR technology was employed to assess the ground deformation of LGF and its surrounding area, using L-band ALOS-1 PALSAR images from 2007 to 2011. The characteristics of ground deformation, relationships between fissure activity and surrounding faults and groundwater exploitation were analyzed. This study shows that the north side of Longyao fault (LF) is uplifting while the south side is subsiding. This provides the tectonic conditions responsible for the activity of the ground fissure. Local groundwater exploitation also plays an important role in the development of ground fissures. InSAR observations were modeled to infer the loading depth (-2.8 km) and the slip rate (31.1 mm/yr) of LF.

1. Introduction

A ground fissure is a type of geo-hazard that occurs naturally on the earth's surface, usually as a discontinuous and broken feature (Geng and Li, 2000; Peng, 2012; Xu et al., 2015). The occurrence of ground fissures is usually associated with either tectonic or human activities. They can be caused by tectonic faulting (Peng et al., 2013), earthquakes (Dou et al., 2005), oil mining, groundwater pumping (Holzer, 1984; Rojas et al., 2002; Pacheco-Martinez et al, 2013.2), and other events. Due to the difference in vertical deformation and horizontal tension between the two sides of a ground fissure, they have the potential to cause great damage to the foundations of dams, buildings, roads, underground pipes and similar structures. The formation of ground fissures not only reduces the value of the land along the cracks, but also causes huge economic loss and has an environmental impact.

Considering the scientific importance and the potential damage which fissures can cause to the environment, studies on the formation mechanism of ground fissure have been conducted numerous times. These studies have been based on both regional tectonic analysis and numerical simulations (Stacey, 1999; Bankher and Al-Harthi, 1999; Peng, 2012). In order to provide a better understanding of the formation mechanism, deformation on the crack and its surrounding environment should be taken into consideration. Many methods can be used to detect and monitor ground fissures, including both geodetic and geophysical approaches. Geodetic methods tend to be focused on deformation monitoring of ground fissures, for example using repeat optical leveling and global positioning system (GPS) surveys. Geophysical methods are usually used to detect the underground location of a ground fissure and its burial depth. This is done through the physical characteristics of the underground medium, for example using ground penetrating radar (GPR) and electrical prospecting.

As a geodetic technique, Interferometric Synthetic Aperture Radar (InSAR) is capable of mapping subtle surface deformation with high spatial resolution, and has been successfully applied to the observation of many geophysical phenomena in past decades, including earthquakes, volcanoes and other geologic processes (e.g., Massonnet et al., 1993; Zebker et al., 1994; Lu et al., 2003; Chaoying et al., 2012; Lingyun et al., 2015; Yang et al., 2016). The InSAR technique can not only monitor the deformation of ground fissures, but also the surrounding area. Therefore, InSAR technology can provide a new tool for monitoring ground fissure activity (Yang et al., 2014a,b; Brunori et al., 2015).

* Corresponding author.
E-mail addresses: ycsgps@163.com (C. Yang), zhonglu@smu.edu (Z. Lu), zhangqinle@263.net.cn (Q. Zhang), zhaocahoying@163.com (C. Zhao), dinsar010@163.com (L. Ji).

https://doi.org/10.1016/j.jag.2017.12.010
Received 13 October 2017; Received in revised form 20 December 2017; Accepted 21 December 2017
Available online 26 December 2017
0303-2434/

The aim of this paper is to contribute to a better understanding of the activity of the LGF and its surroundings. We exploited ALOS PALSAR images (L-band), acquired along an ascending path, to map activity on the Longyao ground fissure (LGF) on the North China Plain. The deformation of the surrounding area was also examined. The StaMPS (Stanford Method for Persistent Scatter) PS-InSAR technique was used to obtain the time series surface deformation (Hooper et al., 2004, 2007). Ground deformation characteristics over the LGF and its surrounding area were obtained. Possible explanations on the observed deformations are then discussed in detail.

This paper is organized as follows: first, the geological setting of the LGF is introduced in Section 2. Then, the StaMPS InSAR technique and ALOS PALSAR data processing are briefly summarized in Section 3. The results are reported and discussed in the subsequent sections (Sections 4 and 5). Modeling results are discussed in the final section.

2. Geological setting of longyao ground fissure

The LGF is located in Xingtai, North China Plain, China. The area is also the core of the North China block. Three geological blocks, the Ningjin-Hengshui Fault Convex, the Xing-Heng Uplift, and the Lin-Qing Graben, meet in this area and form a “Trident” shape in the plane (Fig. 1). There are several north-east and east-west fault zones in this area, among which the main faults are the Taihang Piedmont Fault, and the eastern and western sections of the Shulu Graben. In addition, there are also several secondary ruptures (Jishan et al., 2012). The mainland of China is in a collision and squeezing situation caused by the convergence of the Indian, Eurasian and Pacific plates. Consequently, the North China Plain has suffered long term tensile stress (Furen et al., 2004; Shixiong et al., 2006; Qiang et al., 2008). As a result, more than 1000 cracks spread across the North China Plain. Among these LGF is the longest and most active, with a total length of 36 km (Xuejun et al., 2011; Jishan et al., 2012).

The LGF was initially formed during the Xingtai earthquake in 1966 (Fig. 1). After this the crack entered an inactive period (Jishan et al., 2012). The crack re-exposed in 2003, and the scale and activity of the crack has increased rapidly since 2006 (Jianling et al., 2015). According to field surveys, the fissure was remarkably distributed, appearing in more than 20 villages with a nearly E-W orientation. The maximum width of the crack at the ground surface is 60 cm, and the visible depth is up to several meters (Xu et al., 2015; Peng et al., 2016).

Because LGF is a typical ground fissure disaster in the North China Plain, it has been studied by many experts and scholars. Using a numerical simulation of the tectonic stress field, Ma (2009) concluded that the crack was closely related to seismic activity, and caused by the regional tectonic stress. Wei et al. (2011) pointed out that the crack was caused by fault creep activities and suggested that it was a result of the accumulation and release of tectonic stress. Jishan et al. (2012) suggested that the Longyao fault (LF) provided a source of tectonic engine, and that the crack was the result of the expansion of tensile stress in this system. Current research on LGF is mainly based on the regional tectonic background and numerical simulations, in order to determine the

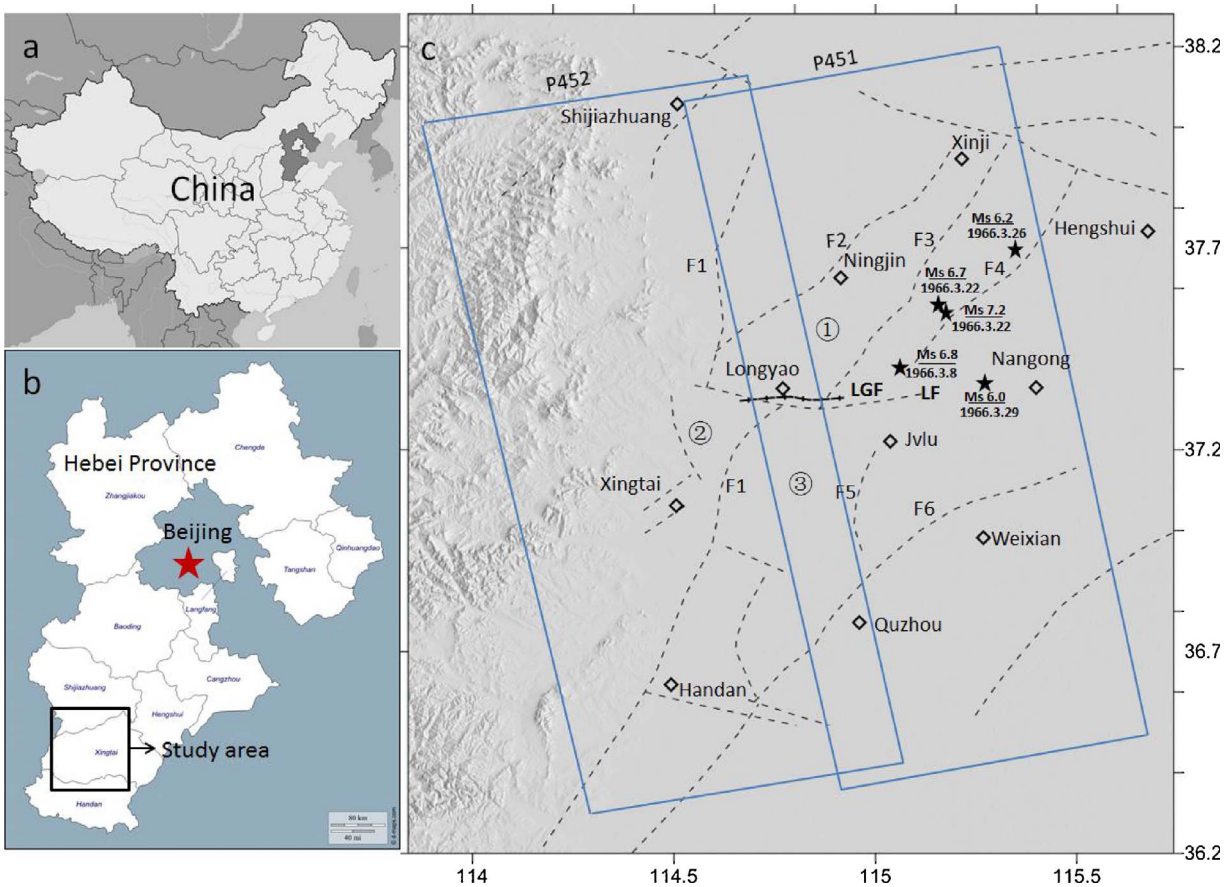

Fig. 1. Shaded relief map of the Longyao ground fissure and its surrounding area. a) A sketch map of Hebei province in China. b) The location of the study area in Hebei province. c) A shaded relief map of the study area. Cities are depicted with small diamonds. The dashed lines indicate the main faults in the region. The light blue solid line boxes show the coverage of ascending ALOS PALSAR image tracks from Path 451 and Path 452. The Longyao fissure is expressed as a black bold line with a cross and labeled as LGF. Faults F1 to F6 represent the Taihang Piedmont Fault, Lincheng Fault, Shulu Graben Western edge Fault, Shulu Graben Eastern edge Fault, Jize Fault and Minghua Fault, respectively. The symbols ① to ③ represent the Ningjin-Hengshui Fault Convex, Xing-Heng Uplift and Lin-Qing Graben, respectively. LGF and LF represent the Longyao ground fissure and Longyao fault. The black stars indicate the locations of the Xingtai earthquake group in 1966. Near the black pentagrams, the digits above the short line indicate the earthquake magnitude, and the digits below the short line indicate the time of earthquake occurrence. (For interpretation of the references to colour in this figure legend, the reader is referred to the web version of this article.)

formation mechanism. However, there is a lack of monitoring data for ground surface deformation in the surrounding area. Therefore, in order to gain a better understanding of the formation mechanism, it is necessary to carry out deformation monitoring of the crack and its surrounding.

3. Methods and data processing

3.1. Methods

The precision of traditional differential InSAR is affected by several factors, such asinaccurate DEM, uneven atmospheric path-delay, and decorrelations related to spatial and temporal changes of the surface scattering properties (e.g., Hanssen, 2001; Lu and Dzurisin, 2014). To reduce the effects of these errors, multi-temporal InSAR (MTInSAR) was proposed. Methods include persistent scatterer InSAR (PSInSAR) (Ferretti et al., 2001; Hooper et al., 2004; Kampes, 2006), the Small BAseline Subset (SBAS) approach (Berardino, 2002; Usai, 2003; Lanari et al., 2004), and the coherent pixel technique (CPT) (Blanco et al., 2008; Mora et al., 2003) among others (e.g., Zhang et al., 2015). In order to understand the time series deformation characteristics of LGF and its surrounding area, the StaMPS (Stanford Method for Persistent Scatterers) was used (Hooper et al., 2004, 2007). The StaMPS uses spatial correlation of interferogram phases to identify PS pixels. This strategy makes it possible to detect PS or slowly decorrelating filtered phase (SDFP) pixels in all terrains. Assumption of temporal variations in the deformation rate is not required (Hooper et al., 2004; Qu et al., 2014). Please refer to Hooper et al. (2004, 2007) for processing details.

3.2. InSAR data and processing

We collected two overlapping ascending tracks of L-band ALOS-1 PALSAR data acquired between 2007 and 2011: 20 acquisitions from path 452 and 17 acquisitions from path 451. Each acquisition consists of 3 consecutive frames. 20100101 and 20100118 (in yyyymmdd) were selected as the master images for Paths 451 and 452, respectively. The temporal-spatial baseline distributions of the interferograms are shown in Fig. 2. Single look complex images were generated using ROI_PAC (Rosen et al., 2000). Interferograms were generated using Doris (Kampes, 2006). The topographic phase was removed from the interferograms with Shuttle Radar Topography Mission (SRTM) 1 arc-sec (30 m) data. The StaMPS PS-InSAR technique was used for InSAR time series analysis of the interferograms. Orbit error and atmospheric phases were estimated and subtracted from differential interferograms during the StaMPS processing. Finally, time series deformation results at each coherent pixel were obtained.

4. Results and analysis

According to the processing procedure mentioned in the previous section, approximately 16 and 19 single-master interferograms were formed from Paths 451 and 452, respectively. Finally, annual ground deformation maps in line-of-sight (LOS) over LGF and its surroundings were assessed from 2007 to 2011. As we already know, LOS deformation acquired by InSAR can be considered as a combination of displacements in east-west, north-south and vertical directions according to the following equation (e.g., Lu and Dzurisin, 2014):

$$V_{los} = [v_{east}\, v_{north}\, v_{vertical}] \begin{bmatrix} -\cos\alpha\cdot\sin\theta \\ \sin\alpha\cdot\sin\theta \\ \cos\theta \end{bmatrix} \quad (1)$$

where α and θ are the azimuth angle of the SAR satellite and the incidence angle, respectively. In our case, α is −10.1° and θ is 38.7°. As a result, $V_{los} = -0.6156v_{east} - 0.1096v_{north} + 0.7804v_{vertical}$. Under the same magnitude of displacement in the three directions, vertical displacement will make a major contribution to the LOS deformation measurement. Past study has shown that horizontal deformation in North China Plain is very small (Wei et al., 2014). Therefore, InSAR LOS deformation on two paths were converted to vertical deformation by $v_{vertical} = V_{los}/\cos\theta$. A mosaic of vertical deformation map from two adjacent satellite tracks (Paths 451 and 452) is shown in Fig. 3. The positive and negative signs represent subsidence and uplift, respectively. Since no prior deformation information is available, the mean value of the InSAR results in the whole image is used as the zero reference value. This is recommended in StaMPS processing when no ground truth is available (Hooper et al., 2013).

4.1. Annual deformation rate

According to the LOS deformation results from the ascending ALOS PALSAR-1, ground subsidence is mainly found in the three regions. These are Jvlu, Ningjin-Xinji and a local area to the east of Longyao (Fig. 3). Subsidence in the Jvlu region is especially serious, and can be seen as a “7” shape. The maximum subsidence rate in this region is up to 60 mm/yr. This deformation occurred at the intersection of the NNE-SSW striking fault (F5) and the near E-W striking fault (LF), i.e., at the turning zone of the two faults. It indicates that the faults play a leading role in the shape of the deformation field, and this effect was most likely to be caused by the blockage of groundwater aquifers by existing faults. The localized subsidence east of Longyao (about 10 km to the north of

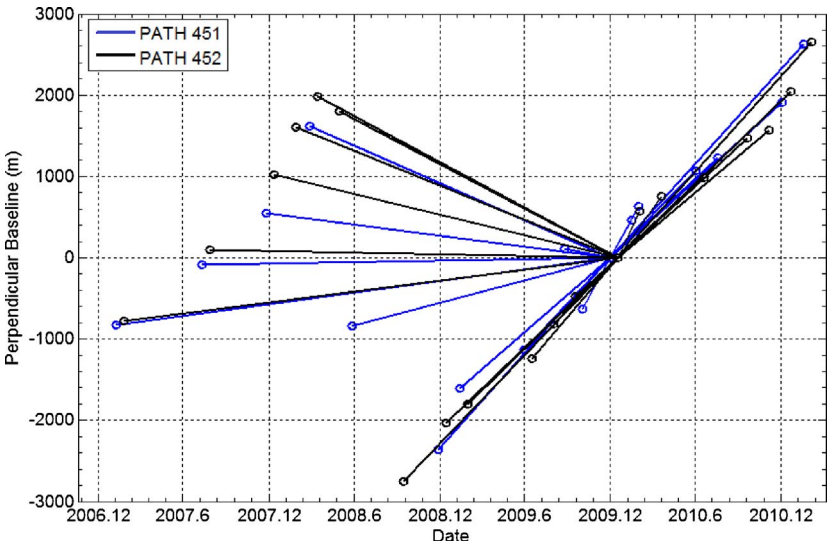

Fig. 2. Baselines of interferograms from Path 451 and Path 452. The Y-axis shows the perpendicular baseline in meters. The image acquisition dates are shown on the X-axis. All of the connecting lines represent interferometric pairs used for time-series analysis.

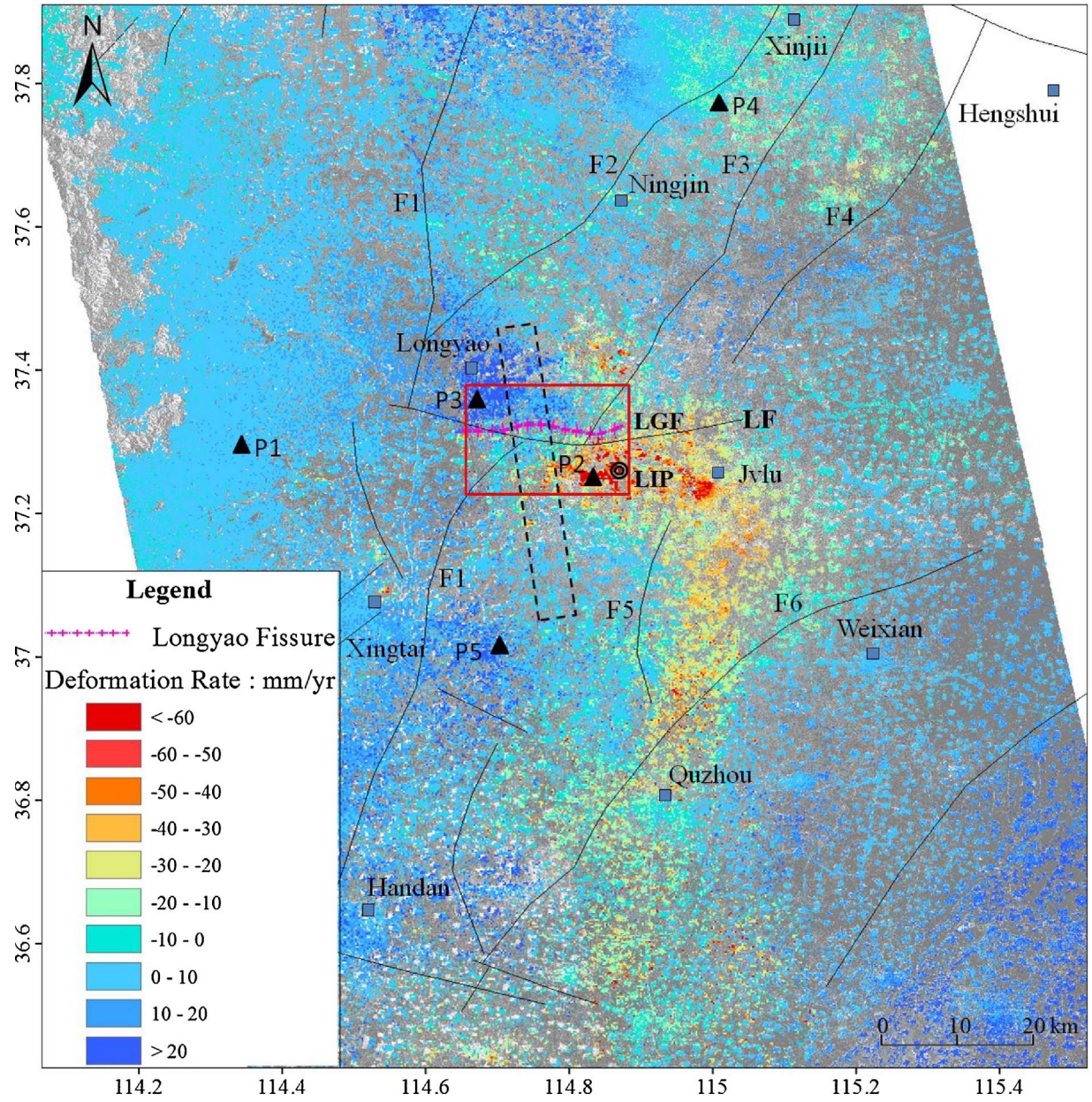

Fig. 3. Annual deformation rates derived from the InSAR time series over the Longyao ground fissure and its surrounding area. P1 to P5 show the positions of the points being used to plot the time series deformation curve in Fig. 4. They represent Jvlu (P1), Longyao (P2), Ningjin (P3), Xingtai (P4) and the mountain area (P5). F1 to F6 represent the major faults described in Fig. 1. The red rectangle is the region shown in Fig. 5. Concentric circles represent the position of the Longyao Industrial Park (LIP). (For interpretation of the references to colour in this figure legend, the reader is referred to the web version of this article.)

LGF) (Fig. 3) was likely caused by ground water pumping. The Ningjin-Xinji area has a subsidence rate of about 20 mm/yr. The InSAR results also show that Longyao town was uplifting during the period from 2007 to 2011. There is also a slight uplift trend near Xingtai, which is located in the transition zone between the Taihang Mountain and the North China Plain (Fig. 1). We suspect that, under the influence of the Taihang uplift (to the west of F1), a differential movement between Xingtai and the North China Plain (to the east of F1) exists, resulting in a relatively slight uplift near Xingtai.

To understand these deformation results, there are two phenomena that deserve our attention:

1) The Longyao fissure is located in the transition zone between subsidence and uplift, where the deformation gradient is the largest. Guangya et al. (2010) suggests that the occurrence of ground fissures is related to subsidence, especially at the edge of the subsidence funnel, where the horizontal tension was greatest.Although two larger settlement centers are located in the research area, they have different deformation features.
2) The NingJin-Xinji settlement center has a smaller subsidence magnitude, and no obvious deformation boundary. The subsidence magnitude of the Jvlu settlement center is significantly larger, and there is a clear boundary. These phenomena suggest that the boundary of deformation in Jvlu may be influenced by external factors, such as regional faults, stratigraphic structure, compression layer thickness and other factors (Zi-yong et al., 2007).

4.2. Time series of deformation

The StaMPS PS-InSAR procedure allowed the estimation of time series deformation data for each of the coherent points identified in the SAR scene. Therefore, a time series of deformation was extracted for

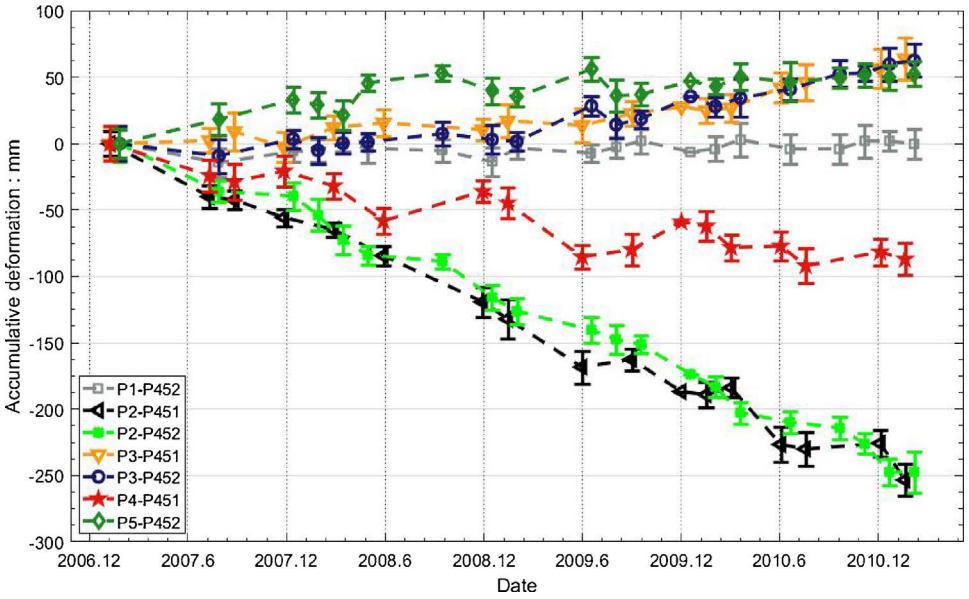

Fig. 4. Accumulated subsidence curves. 'P1-P452' represents the deformation derived at P1 from P452. 'P2-P451' and 'P2-P452' represent the deformations observed at P2 from paths 451 and 452, respectively. 'P3-P451' and 'P3-P452' represent the deformation observed at P3 from paths 451 and 452, respectively. 'P4-P451' represents the deformation observed at P4 from path 451. 'P5-P452' represents the deformation observed at P5 from path 452. The locations of P1 to P5 can be found in Fig. 3. The lengths of the I-symbols superimposed on the time series plots represent the standard deviations of the deformation measurements.

five points, which are P1 to P5 (shown as triangles in Fig. 3). Due to the slight difference in the deformation measurement between the neighboring PS points, we averaged the rates of all PS points within a square of 500 m × 500 m. This produced a final deformation measurement for each of the selected regions. The standard deviation of the deformation measurements within the square was calculated at the same time, and is shown as the error bar in Fig. 4. For the purpose of comparing the consistency of two adjacent paths, the InSAR results within the common coverage area of paths 451 and 452 were extracted and converted into vertical components, using their incidence angles (Fig. 4). The cumulative uplift values around Longyao (P3) and Xingtai (P5) were 60 mm and 50 mm, respectively, during the period from 2007 to 2011. The annual average uplift rates were approximately 15 mm/yr and 12 mm/yr, respectively. Deformation was nearly steady from January 2007 to January 2009 in the Longyao area, while it showed a clear linear upward trend from January 2009 to February 2011 for unknown reasons. The cumulative subsidence values at P2 and P4 were 250 mm and 80 mm, respectively, during the period from 2007 to 2011. The annual average subsidence rates were approximately 65 mm/yr and 20 mm/yr, respectively at these sites.

4.3. Ground fissure deformation

The activity characteristics of ground fissures are usually complex. Activity occurs in an intermittent fashion in space and intermittently in time. The detailed deformation over red rectangle in Fig. 3 is shown in Fig. 5. It can be seen that the deformation rates between the two sides of the ground fissure are different from one part to another. This difference is particularly obvious in the eastern part of the crack.

The pink crossed line in Fig. 5 is the location of the LGF as obtained from field investigations. The black line is the location of the LF. Deformation measurements at coherent points along two lines (R1 and R2) near the LGF show discontinuous deformation rates. Both lines are roads surrounded by agricultural fields. According to the location of LGF (Fig. 5) and our field investigation, the location of the discontinuous deformation rates is exactly LGF. Field investigation photos are also shown in Figs. Fig. 55(b) and Fig. 55(c). The ground scarp formed by the deformation of the ground fissures can clearly be seen in these photos. Deformation rates from path 451 and 452 were extracted from points A to B along road R1. These are shown in Fig. 6. The deformation rate profiles were found to be very consistent with one another. The ground deformation rate had an obvious gradient of approximately 40 mm/yr between the two sides of the crack. According to the spatial distance of the deformation gradient, the influence width of the crack at this cross-section was more than 400 m. It should be noted that there might be a branch of the ground fissure to the east of the road (R1). The possible location of this branch has been marked with a thick blue break line. The deformation in the northern block is basically stable, while significant subsidence is occurring in the southern block. A significant deformation gradient also appeared on the road (R3), which has similar deformation characteristics to R1 and R2.

According to leveling measurement results, carried out from 2013 to 2014, the difference in deformation rates between the two sides of the crack were 12 mm/yr and 48 mm/yr in Zhouzhang village and Xidianzi village (Fig. 5), respectively (Jianling et al., 2015). Our InSAR measurements at two sites show the differences are 10 mm/yr and 40 mm/yr, respectively. Although the leveling and InSAR results were carried out at different times, they are generally consistent in magnitude. Both results showed that the ground fissure was more active in the eastern section of the LGF than in the western section where groundwater induced subsidence is much less (Fig. 3).

5. Discussion

5.1. Ground fissure activity and groundwater

Groundwater in the Longyao region is in a state of over-exploitation, causing groundwater levels to decline at an ever increasing rate. According to the report (Jianling et al., 2015), the depth of the groundwater level in Xidianzi village (Fig. 5) decreased from 2 m to 20 m in the period from 1959 to 1992. The average rate of decline was 0.54 m/yr (Jianling et al., 2015). Up to 2013, the underground water level at Xidianzi dropped to 52 m, with an average decline rate of 1.52 m/yr (Jianling et al., 2015). Hence, the groundwater decline rate has tripled over the last 20 years. It is important to note that the subsidence center, adjacent to the eastern end of the LGF, is the Longyao Industrial Park (LIP), which was established in November 2003 (Fig. 3). The main products of the LIP are instant noodles and beverages. Its annual production consists of 1.1 million tons of instant noodles, 1 million tons of drinks and 200 million cups of milk tea (https://baike.so.com/doc/1075234-1137813.html, visited on September 15, 2017). In addition, various kinds of food and light industrial products are also produced. These industrial processes consume large amounts of groundwater. The time at which accelerated activity occurred on the LGF is very consistent with the time at which the industrial park was set up. This highlights the role that groundwater exploitation plays in

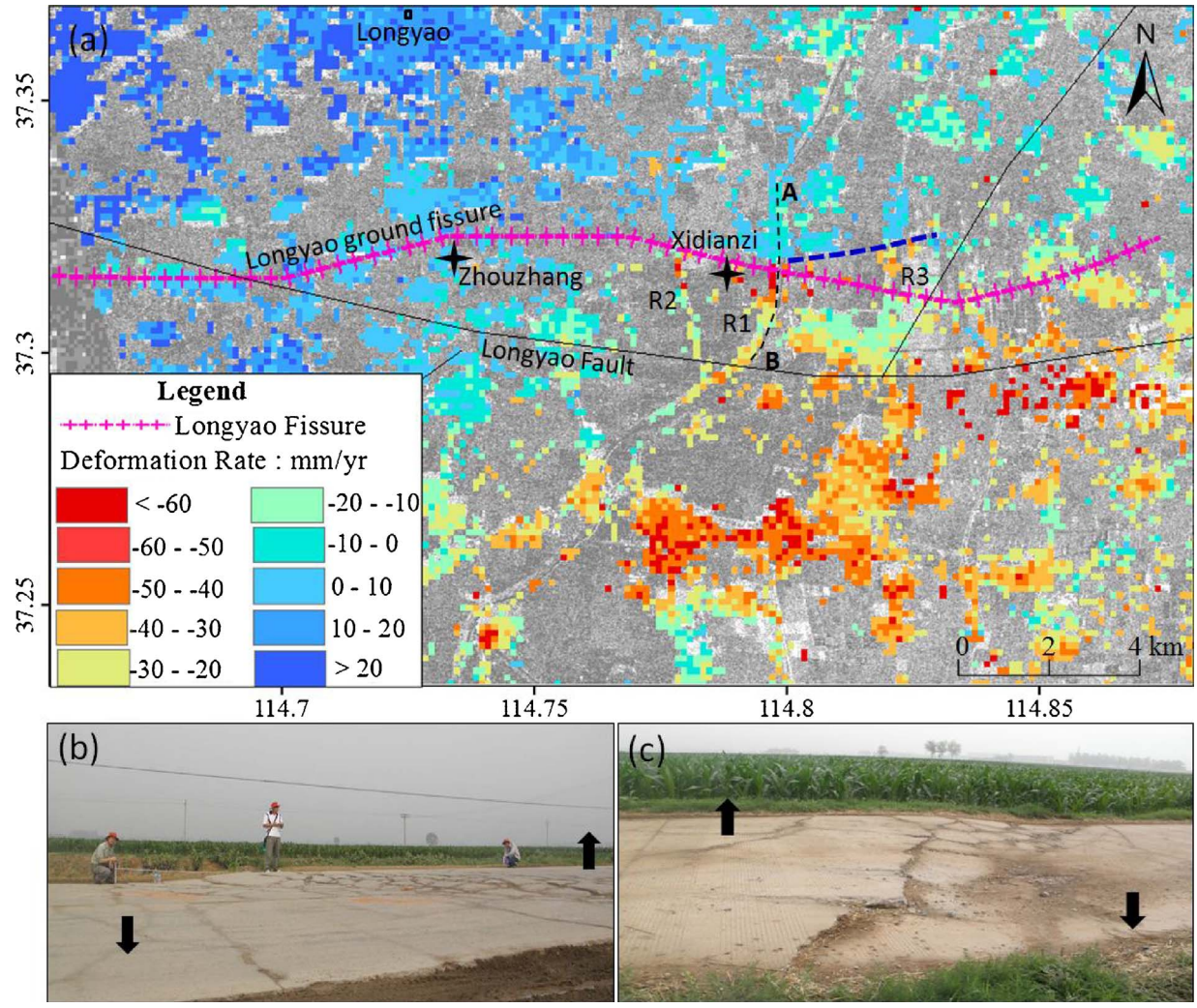

Fig. 5. a) Ground deformation rates over the ground fissure region derived from P451. b) Field investigation photo of road 1 (R1). c) Field investigation photo of road 2 (R2). The bold black arrows show the relative movement direction of the two sides of the ground fissures).

accelerating the activities of the LGF.

Several studies have shown that the existence of the fault may act as a water barrier and thus affect groundwater migration (Lu and Danskin, 2001; Donnelly et al., 2008; Brunori et al., 2015). The mechanical strength of soil on the existing fault zone is weak. As a result, the soil will easily slip and crack along the fault zone when underground water pumping takes place (Zhenwei et al., 2012). This means that the LF and underground water pumping have a beneficial effect on the activity of the LGF.

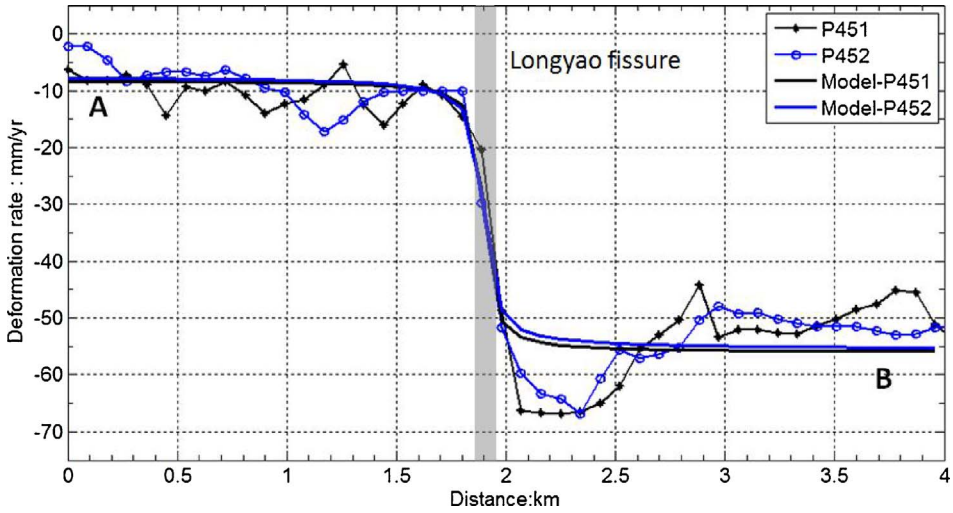

Fig. 6. Deformation rate profiles across the ground fissure. The gray wide line shows the location of the fissure. A and B represent the direction of the profile as shown in Fig. 5.

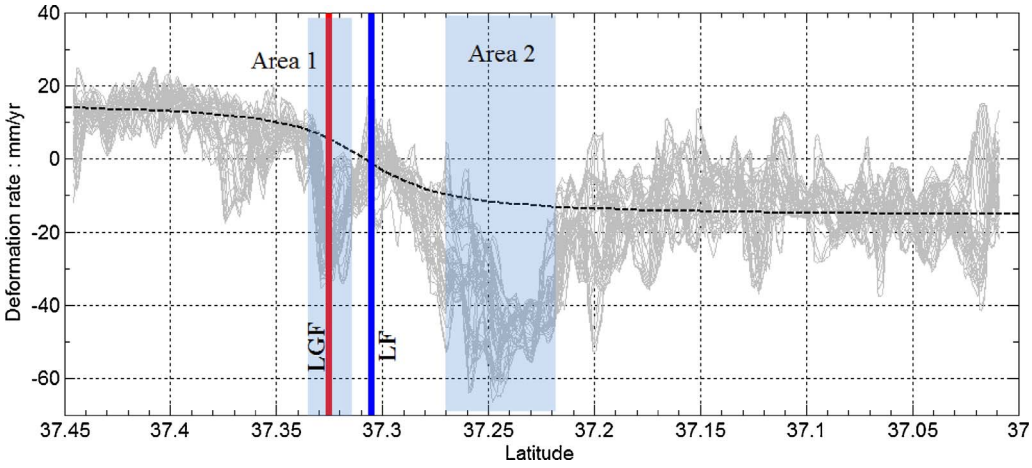

Fig. 7. Deformation rate profiles crossing the LF. The grey lines represent the deformation profiles along the dashed black box shown in Fig. 3. Areas 1 and 2 represent the region affected by the ground fissure and the pumping-induced subsidence area, respectively. The red and blue lines represent the positions of the Longyao ground fissure (LGF) and Longyao fault (LF), respectively. Black dashed line represents the model results from Eq. (2). (For interpretation of the references to colour in this figure legend, the reader is referred to the web version of this article.)

5.2. Ground fissure activity and regional stress

There may be multiple causes for the activity along the LGF. In addition to underground water pumping, we believe that the regional stress has a certain role in promoting LGF activity. Both the field investigation and InSAR results show that the north blocks of the LF and LGF are rifted upwards, relative to the southern one that declines (Fig. 3). The LGF is located in the transitions zone between the Xing-Heng Uplift block to the north and the Lin-Qing Graben to the south. The profile of ground surface displacement across the LF is shown in Fig. 7. The northern segments of the profiles have an uplift trend relative to the southern segments. This is consistent with existing stratigraphic profile data (Wanghe, 1987). Two settlement funnels in the profiles (Areas 1 and 2 in Fig. 7), correspond to the areas affected by the ground fissure and the pumping-induced subsidence, respectively. These profiles show that the motion of the blocks still has an effect on the surface deformation, which provides the conditions for the activity on the LGF.

Moreover, studies on the Fenwei basin have shown that the ground fissures within this area are mainly controlled by the surrounding continental dynamics and that excessive pumping of groundwater is a positive factor for promoting their activity (e.g., Peng et al., 2007). The North China Plain is adjacent to the Fenwei basin, and they have a similar regional tectonic stress field (Jishan et al., 2012). Therefore, the LGF should also be affected by the regional tectonic stress.

5.3. Is LF responsible for the opening of LGF?

Several studies have shown that the formation and opening of ground fissure are related to hidden faults (Wesley Peirce, 1979; Quanzhong et al., 2013; Brunori et al., 2015). Under the combination of tectonic and human factors, hidden faults begin to expand upward. When the absorption effect of the overlying strata is insufficient to resist the expansion, the crack is generated. The opening of LGF is also considered to be related to the hidden fault, which is the LF. There are several reasons to support our opinions:

1) According to our field investigation, the destructive, exposed, segments of the LGF are linear and oriented with the strike of the LF, proving that the LGF is closely related with the LF.
2) The LGF formed during the Xingtai earthquake group (Fig. 1), when 5 earthquakes with Ms ≥6.0 occurred within 21 days. Consequently, we speculate that the intensive earthquakes may have caused the LF to slide and so caused the appearance of the LGF. Ground cracks induced by earthquakes have been reported elsewhere (Dou et al., 2005; Konagai et al., 2016).
3) Several trenches that across the LGF have been explored. The sections of the trenches show that the extension of LGF in the deep is connected to the LF (Jishan et al., 2012). In addition, the fillings of LGF are multi-staged, meaning that there have been many activities in history (Peng et al., 2016).
4) As revealed by our InSAR result (Fig. 6), the LGF and LF have the same characteristics, i.e., the southern fault block drops and the northern fault block uplifts. In addition, our field investigation has shown that LGF has a left-lateral sliding characteristic, which is consistent with that of LF. The groundwater pumping alone cannot lead to strike-slip motions in the horizontal.

6. Modeling profile velocities of the fault and ground fissure

Many studies have shown that geodetic observations across active faults can be explained by creeping dislocations buried in an elastic homogeneous half-space (Vergne et al., 2001; Biggs et al., 2008; Hussain et al., 2016). The ground deformation across an active fault can be modeled as an arctangent, which provides an estimate of both the slip rate of the fault and its locking depth. A simple model of this movement for vertical strike slip faults is a homogenous elastic half space (Savage and Burford, 1973). This can be described as:

$$V(x) = \frac{S}{\pi}\arctan\left(\frac{x}{D}\right) + \alpha \quad (2)$$

where $V(x)$ is the fault-parallel velocity of points estimated along a perpendicular profile across the fault, x is the distance from the fault, S is the fault slip rate, D is the dislocation depth, and α is a static offset.

To better understand the ground deformation across LF, the above model was used to model the InSAR deformation profiles in Fig. 7. The results in areas 1 and 2 (Fig. 7), caused by ground fissure activity and groundwater pumping, respectively, were removed to avoid the impact on creeping dislocations on the model. Taking into account the geological observation, the latitude of 37.3° was considered to be the location of the fault, for the purposes of calculating x in formula (3). We found the best fit values for each model parameter (S, D and α) using a Markov chain Monte Carlo (MCMC) sampler algorithm (Haario et al., 2006; Hussain et al., 2016). This algorithm samples the target distribution using a Markov chain with a steady distribution. It ensures that the correct samples are collected to build the desired posterior distribution. The MCMC sampler explores the parameter space constrained by $-100 < S$ (mm/yr) < 0, $-50 < D$ (km) < 0 and $-100 < \alpha$ (mm/yr) < 100, assuming a uniform prior probability distribution over each range.

In total, we produced more than 30,000 independent model parameter solutions. Fig. 8 (bottom) shows the frequency histograms for each model parameter. The probability distributions for the fault slip rate, the locking depth, and the static offset are approximately normally

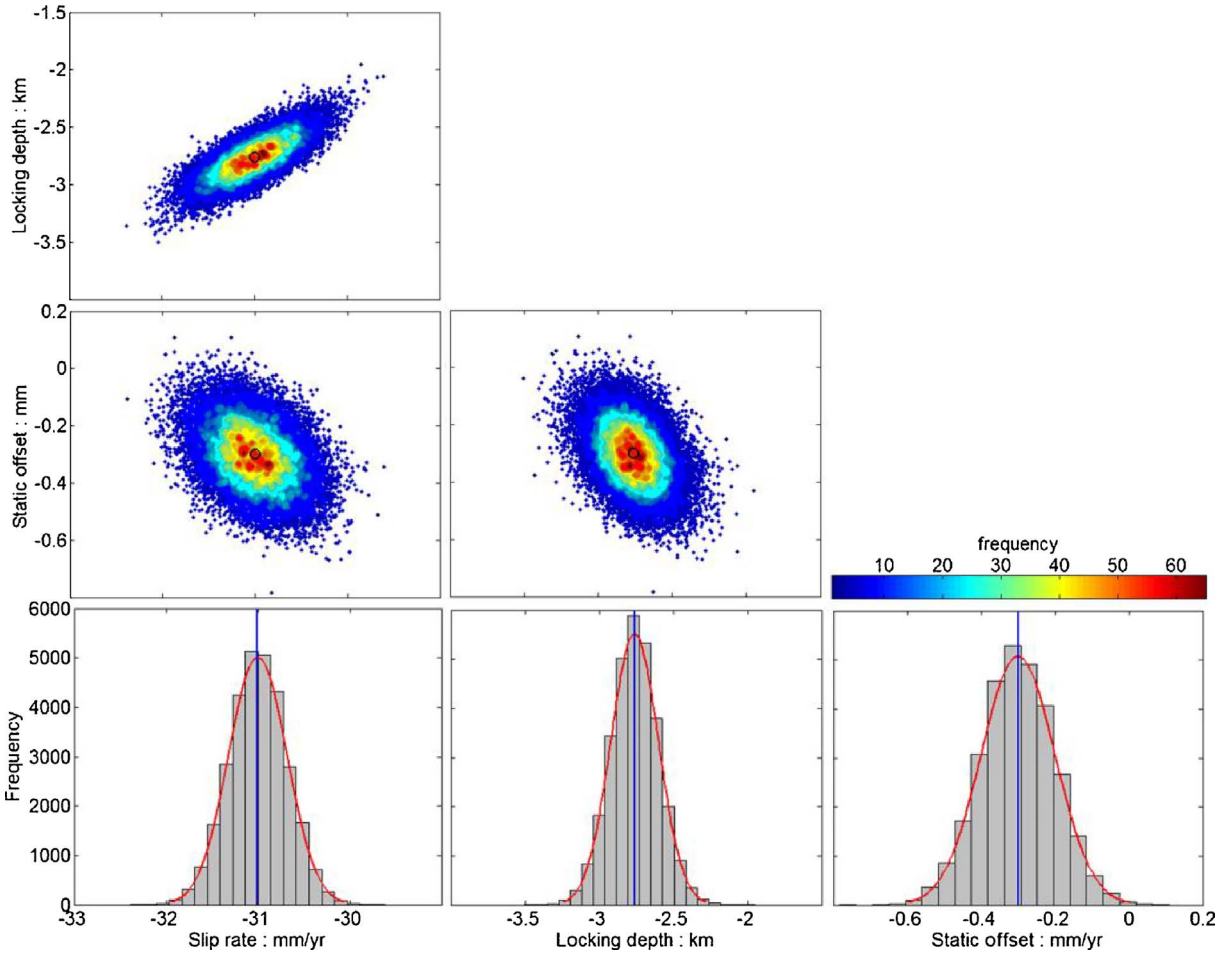

Fig. 8. Bootstrap analysis and frequency histograms for modeled parameters, for profiles across the LF. The optimal solution for the parameters is estimated from the mean value (the blue vertical line) of the best-fit Gaussian distribution (the red curve).The dots indicate the parameter solutions that were selected. (For interpretation of the references to colour in this figure legend, the reader is referred to the web version of this article.)

distributed. The remainder panels in Fig. 8 show two-dimensional confidence regions for parameter pairs. All of the model parameters are well constrained according to the bootstrap analysis. The optimal solutions for the parameters are estimated from the mean value (the blue vertical line in Fig. 8): a fault slip rate of −31.1 mm/yr and a depth of −2.8 km. The modeled profile for LF is shown as the black dotted line in Fig. 7. It is worth noting that the simple model used assumes that the dip angle is 90°, which is often not the case in reality. According to seismic exploration data, the dip angle of the LF is 70–80 ° (Jun et al., 2011). Although this is a potential source of error, the simple elastic dislocation model matches the profile well, and is able to give a first-order estimate of the fault slip rate and locking depth. Finally, we note that the locking depth of the best fitting model is very consistent with that of the geological survey data (Wanghe, 1987).

Using the same method, the dislocation depths for the ground fissure are found to be 30 m and 40 m, based on InSAR observations from paths 451 and 452, respectively. Both of the slip rates are −48 mm/yr. The modeling results are shown as solid lines in Fig. 6. The model results from the two paths match each other very well. According to the model results, the cracks exist in the shallow soil layer within 40 m of the surface, which agrees with that from our field investigations.

7. Conclusion

The LGF and its surrounding areas are one of the most complex geologic environments in China. Fault activity, ground fissures, and land subsidence have all occurred in this region. In this paper, PS-InSAR technology was employed to assess the ground deformation of LGF and its surrounding area. ALOS PALSAR images, for the period from 2007 to 2011 were used. The characteristics of ground deformation were analyzed, as was the relationship between the fissure activity, surrounding faults and groundwater exploitation. Both the InSAR results and the geological data show the same plate movement characteristics: the north side of LF is in uplift and south side is in subsidence. This indicates that the sustained action of plate motion provides the conditions for the ground fissure activity. At the same time, groundwater exploitation has played an important role in the activity of LGF. By extracting deformation profiles perpendicular to the ground fissure, we show that there is an obvious deformation gradient of approximately 40 mm/yr between the two sides of the crack. A simple model in a homogenous elastic half space was used to model the influence of the existing fault on the regional deformation. For profiles across the LF, a locking depth of −2.8 km and a far field fault slip velocity of −30.1 mm/yr are the best fit model parameters.

Acknowledgments

We are grateful for the helpful corrections and suggestions made by the Editor-in-Chief and two anonymous reviewers. This research was funded jointly by the National Natural Science Foundation of China (NSFC) (Nos. 41731066, 41628401 and 41604015), the Special Earthquake Research Project of China (No. 201508009), the National Program on Key Basic Research Project (973 Program) (Grant No. 2014CB744703), the Fundamental Research Funds for the Central

Universities (310826161017), the China Scholarship Council, and the Shuler-Foscue Endowment at Southern Methodist University. We also thank JPL/Caltech for ROI PAC, TU-Delft for DORIS, and Andy Hooper for StaMPS.

References

Bankher, K.A., Al-Harthi, A.A., 1999. Earth fissuring and land subsidence in western Saudi Arabia. Nat. Hazards 20 (1), 21–42.

Berardino, P., 2002. A new algorithm for surface deformation monitoring based on small baseline differential SAR interferograms. IEEE Trans. Geosci. Remote Sens. 40, 2375–2383.

Biggs, J., Burgmann, R., Freymueller, J., Lu, Z., Parsons, B., Ryder, I., Schmalzle, G.M., Wright, T., 2008. The postseismic response to the 2002 M7.9 denali fault earthquake: constraints from InSAR. Geophys. J. Int. 175 (3). http://dx.doi.org/10.1111/j.1365-246X.2008.03932.

Blanco, P., Mallorquí, J.J., Duque, S., Monells, D., 2008. The coherent pixels technique (CPT): an advanced DInSAR technique for non-linear deformation monitoring. Pure Appl. Geophys. 165, 1167–1193.

Brunori, Carlo Alberto, Bignami, Christian, Albano, Matteo, Zucca, Francesco, Samsonov, Sergey, Groppelli, Gianluca, Norini, Gianluca, Saroli, Michele, Stramondo, Salvatore, 2015. Land subsidence, ground fissures and buried faults: inSAR monitoring of ciudad guzmán (Jalisco, Mexico). Remote Sens. 7, 8610–8630. http://dx.doi.org/10.3390/rs70708610.

Chaoying, Zhao, Lu, Zhong, Zhang, Qin, de La Fuente, Juan, 2012. Large-area landslide detection and monitoring with ALOS/PALSAR imagery data over northern california and southern oregon, USA. Remote Sens. Environ. 124, 348–359. http://dx.doi.org/10.1016/j.rse.2012.05.025.

Donnelly, L.J., Culshaw, Martin, Bell, F., 2008. Longwall mining-induced fault reactivation and delayed subsidence ground movement in British coalfields. Q. J. Eng. Geol. Hydrogeol. 41 (3), 301–314. http://dx.doi.org/10.1144/1470-9236/07-215.

Dou, A.X., Wang, X.Q., Ding, X., Wang, D.L., 2005. Extraction of ground fissures caused by earthquake MS 6.8 in bachu-jiashi area, geoscience and remote sensing symposium, 2005. IGARSS '05. proceedings. 2005. IEEE Int. 7, 5053–5055.

Ferretti, A., Prati, C., Rocca, F., 2001. Permanent scatterers in SAR interferometry. IEEE Trans. Geosci. Remote Sens. 39, 8–20.

Furen, Xie, Xiaofeng, Cui, Jiantao, Zhao, Qunce, Chen, Hong, Li, 2004. Regional division of the recent tectonic stress field in China and adjacent areas. Chin. J. Geophys. 47 (4), 654–662.

Geng, Da-yu, Li, Zhong-sheng, 2000. Ground fissure hazards in USA and China. Acta Seismol. Sin. 13 (Number 4/July), 466–476.

Guangya, Wang, Jun, Yu, Shuliang, Wu, Jianqiang, Wu, Kaihong, Zong, 2010. Research on the Depth of Earth Fissures in Su-Xi-Chang 8. Urban Geological Environment and Sustainable Development Forum, Shanghai, China, pp. 23–26.

Haario, H., Laine, M., Mira, A., Saksman, E., 2006. DRAM: efficient adaptive MCMC. Statis. Comput. 16, 339–354. http://dx.doi.org/10.1007/s11222-006-9438-0.

Hanssen, R., 2001. Radar Interferometry: Data Interpretation and Error Analysis. Springer, New York.

Holzer, L.T., 1984. Ground failure induced by groundwater withdrawal from unconsolidated sediment. In: In: HoIzer, L.T. (Ed.), Man Induced Land Subsidence, Reviews in Engineering Geology 6. The Geological Society of America, Boulder, Colorado, pp. 67–105.

Hooper, A., Zebker, H., Segall, P., Kampes, B., 2004. A new method for measuring deformation on volcanoes and other natural terrains using InSAR persistent scatterers. Geophys. Res. Lett. 31, 275–295.

Hooper, A., Segall, P., Zebker, H.A., 2007. Persistent scatterer interferometric synthetic aperture radar for crustal deformation analysis. J. Geophys. Res. 112, 1–21.

Hooper, Andrew, Bekaert, David, Spaans, Karsten, 2013. Stamps/MTI Manual Version 3.3b1. University of Leeds, United Kingdom.

Hussain, E., Hooper, A., Wright, T.J., Walters, R.J., Bekaert, D.P.S., 2016. Interseismic strain accumulation across the central North Anatolian Fault from iteratively unwrapped InSAR measurements. J. Geophys. Res. Solid Earth 121, 9000–9019. http://dx.doi.org/10.1002/2016JB013108.

Jianling, Cao, Shufang, Bai, Zhengyi, Jiang, 2015. Characteristic and mechanism analysis of ground fissure in longyao. North China Earthquake Sci. 33 (2), 13–19 (in Chinese).

Jishan, Xu, Jianbing, Peng, Xuejun, Ma, Runyong, Ma, Xudong, Yang, Shaowu, Feng, Haibo, An, 2012. Characteristic and mechanism analysis of ground fissures in longyao, Xingtai. J. Eng. Geol. 20 (2), 160–169.

Jun, Feng, Hongguang, Li, Tao, Wu, Yue, Xuan, Weihua, Li, 2011. Geochemical survey of Longyao concealed fault in Hebei. Geophys. Geochem. Explor. 35 (5), 597–599.

Kampes, B.M., 2006. Radar Interferometry, Persistent Scatterer Technique 12 Springer, Berlin, Germany.

Konagai, Kazuo, Kiyota, Takashi, Shiga, Masataka, Tomita, Hikaru, Okuda, Hiroki, Kajihara, Kazuhiro, 2016. Ground fissures that appeared in aso caldera basin in the 2016 kumamoto earthquake, Japan. JSCE J. Disaster Fact Sheets (FS2016-E-0003).

Lanari, R., Mora, O., Manunta, M., Mallorqu, J.J., Berardino, P., Sansosti, E., 2004. A small-baseline approach for investigating deformations on full-resolution differential SAR interferograms. IEEE Trans. Geosci. Remote Sens. 42, 1377–1386.

Lingyun, Ji, Liwei, Liu, Ming, Hao, 2015. Crustal deformation characteristics of zhenkang-yongde region in southwest yunnan observed by InSAR technology. J. Seismol. Res. 38 (1), 84–89.

Lu, Z., Danskin, W., 2001. InSAR analysis of natural recharge to define structure of a ground-water basin San Bernardino, California. Geophys. Res. Lett. 28 (13), 2661–2664.

Lu, Z., Dzurisin, D., 2014. InSAR Imaging of Aleutian Volcanoes: Monitoring a Volcanic Arc from Space: Springer Praxis Books, Geophysical Sciences. Springer, pp. 390 ISBN 978–3-642–00347-9.

Lu, Zhong, Fielding, Eric, Patrick, Matthew, Trautwein, Charles, 2003. Estimating lava volume by precision combination of multiple baseline spaceborne and airborne interferometric synthetic aperture radar: the 1997 eruption of okmok volcano, alaska. IEEE Trans. Geosci. Remote Sens. 41 (6), 1428–1436. http://dx.doi.org/10.1109/TGRS.2003.811553.

Ma, Run-yong, 2009. The North China Plain Typically Cracks Development Areas Active Fault Survey and Tectonic Stress Field Numerical Simulation. (Xian).

Massonnet, Didier, Rossi, Marc, Carmona, César, Adragna, Frédéric, Peltzer, Gilles, Feigl, Kurt, Rabaute, Thierry, 1993. The displacement field of the landers earthquake mapped by radar interferometry. Nature 364, 138–142. http://dx.doi.org/10.1038/364138a0.

Mora, O., Mallorquí, J.J., Broquetas, A., 2003. Linear and nonlinear terrain deformation maps from a reduced set of interferometric SAR images. IEEE Trans. Geosci. Remote Sens. 41, 2243–2253.

Pacheco-Martinez, J., Hernandez-Marin, M., Burbey, T.J., Gonzalez-Cervantes, N., Ortiz-Lozano, J.A., Zermeno-De-Leon, M.E., Solis-Pinto, A., 2013. Land subsidence and ground failure associated to groundwater exploitation in the Aguascalientes Valley. Mexico.Eng. Geol. 164, 172–186.

Peng, J.B., Fan, W., Li, X.A., Wang, Q.L., Feng, X.J., Zhang, J., Li, X.S., Lu, Q.Z., Huang, Q.B., Ma, R.Y., Lu, Y.D., 2007. Some key questions in the formation of ground fissures in the Fen-Wei Basin. J. Eng. Geol. 15 (4), 433–440.

Peng, J.B., Chen, L.W., Huang, Q.B., Men, Y.M., Fan, W., Yan, J.K., 2013. Physical simulation of ground fissures triggered by underground fault activity. Eng. Geol. 155, 19–30.

Peng, Jianbing, Xu, Jishan, Ma, Runyong, Wang, Feiyong, 2016. Characteristics and mechanism of the Longyao ground fissure on North China Plain, China. Eng. Geol. 214, 136–146.

Peng, J., 2012. The Hazard of Xi'an Ground Fissures. Science Press Beijing, China.

Qiang, Sun, Jihong, Yang, Siqing, Qin, Tianba, Liu, Xiuhong, Hu, 2008. Micro-structural analysis of the ground fissures in Hebei plains. J. Eng. Geol. 16 (2), 201–205.

Qu, F.F., Zhang, Q., Lu, Z., Zhao, C.Y., Yang, C.S., Zhang, J., 2014. Land subsidence and ground fissures in Xi'an, China 2005–2012 revealed by multi-band insar time-series analysiss. Remote Sens. Environ. 150, 366–376. http://dx.doi.org/10.1016/j.rse.2014.09.008.

Quanzhong, Lu, Fukun, Zhao, Jianbing, Peng, Feng, Bo, 2013. Overview on rupture propagation studies of buried ground fissures. J. Eng. Geol. 21 (6), 898–907.

Rojas, E., ArZate, J., Arroyo, M., 2002. A method to predict the group fissuring and faulting caused by regional groundwater decline. Eng. Geol. 5 (4), 245–260.

Rosen, P.A., Hensley, S., Joughin, I.R., Li, F.K., Madsen, S.N., Rodriguez, E., Goldstein, R.M., 2000. Synthetic aperture radar interferometry. Proc. IEEE 88, 333–382.

Savage, J., Burford, R., 1973. Geodetic determination of relative plate motion in central California. J. Geophys. Res. 78, 832–845.

Shixiong, Li, Shouding, Li, Hongqiang, Hao, 2006. The distribution characters and origin mechanics of ground fissures hazard in Hebei plain. J. Eng. Geol. 14 (2), 178–183.

Stacey, T.R.F.G., 1999. The influence of subsidence on planning and development in Johannesburg South Africa. Environ. Eng. Geosci. 373–388.

Usai, S., 2003. A least squares database approach for SAR interferometry data. IEEE Trans. Geosci. Remote Sens. 41, 753–760.

Vergne, J., Cattin, R., Avouac, J., 2001. On the use of dislocations to model interseismic strain and stress build-up at intracontinental thrust faults. Geophys. J. Int. 147, 155–162.

Wanghe, Chen, 1987. Quaternary Geology of Hebei Province. Geological publishing, Beijing.

Wei, Song, Xuejun, Ma, Guoxin, Jia, 2011. Cause analysis of creep type ground fissure for Longyao typical faults in Xingtai. Chin. J. Geol. 35 (4), 405–412.

wei, Wang, Dijin, Wang, Bin, Zhao, Yong, Huang, Caihong, Zhang, Kai, Tan, Shaomin, Yang, 2014. Horizontal crustal deformation in Chinese Mainland analyzed by CMONOC GPS data from 2009 to 2013. Geodesy Geodynamics 5 (3), 41–45.

Wesley Peirce, H., 1979. Subsidence fissures and faults in Arizona. Bur. Geol. Miner. Technol. 9 (2), 1–6.

Xu, J., Meng, L., An, H., Wang, L., 2015. The bending mechanism ofanping ground fissure in the Hebei Plain, North China. Environ. Earth Sci. 74 (9), 6859–6870. http://dx.doi.org/10.1007/s12665-015-4670-6.

Xuejun, Ma, Wei, Song, Honglei, Wang, Weiwei, Zhang, Xudong, Yang, Guoxin, Jia, 2011. Causes for the ground cleave in longyao county. J. Geol. Hazards Environ. Preserv. 22 (3), 43–46.

Yang, Cheng-sheng, Zhang, Qin, Zhao, Chao-ying, Wang, Qing-liang, Ji, Ling-yun, 2014a. Monitoring land subsidence and fault deformation using the small baseline subset InSAR technique: a case study in the Datong Basin, China. J. Geodyn. 75, 34–40.

Yang, C.S., Zhang, Q., Zhao, C.Y., Wang, Q.L., Ji, L.Y., 2014b. Monitoring land subsidence and fault deformation using the small baseline subset InSAR technique: a case study in the Datong Basin, China. J. Geodyn. 75, 34–40.

Yang, C.S., Zhang, Q., Xu, Q., Zhao, C.Y., Peng, J.B., Ji, L.Y., 2016. Complex deformation monitoring over the Linfen–Yuncheng basin (China) with time series InSAR technology. Remote Sens. 8, 284.

Howard, Howard A., Rosen, Paul A., Goldstein, Richard M., Gabriel, Andrew, Werner, Charles L., 1994. On the Derivation of Coseismic Displacement Fields Using Differential Radar Interferometry: The Landers Earthquake. J. Geogr. Res. 99 (B10), 19617–19634. http://dx.doi.org/10.1029/94JB01179.

Zhang, L., Ding, X.L., Lu, Z., 2015. Ground deformation mapping by fusion of multi-temporal interferometric synthetic aperture radar images: a review. Int. J. Imaged Data Fusion 6 (4), 289–313. http://dx.doi.org/10.1080/19479832.2015.1068874.

Zhenwei, Jiang, Jianbing, Peng, Qiyao, Wang, 2012. Numerical simulation of the effect of preexisting fault on land subsidence and ground fissures during pumping. J. Jilin Univ. (Earth Sci. Ed.) 42 (4), 1099–1103.

Zi-yong, Sun, Teng, Ma, Jun, Ma, Rui, Ma, Chun-miao, Yan, 2007. Effect of strata heterogeneity on spatial pattern of land subsidence in Taiyuan City. Rock Soil Mech. 28 (2), 399–403.